ADVANCED ELECTRONIC MATERIALS
www.advelectronicmat.de

Bi-Stable Resistance Generation Mechanism for Oxygenated Amorphous Carbon-Based Resistive Random-Access Memory

*Soo-Min Jin, Hea-Jee Kim, Dae-Seong Woo, Sung-Mok Jung, Dong-Eon Kim, Tae-Hun Shim, and Jea-Gun Park**

The oxygenated amorphous carbon (α-CO_x)-based resistive random-access memory (ReRAM) generates a bi-stable resistance via electroforming or the rupture of the conductive C—C sp^2 covalent bond filaments in the α-CO_x resistive layer, which can be determined by the dependency of the intensity distribution of the oxygen ion (O^{2-}), for the 3D cross-point nonvolatile memory as the new memory hierarchical structure for an artificial neural network. The conductive C—C sp^2 and insulating C—C sp^3 covalent bonds are formed near the top of the resistive layer by drifting and diffusing O^{2-} toward the bottom and top parts of the layer in the set and reset processes, respectively. The reset process has a different bi-stable resistance generation mechanism from binary metal oxide-based ReRAM and conductive bridge random-access memory. The conductive C—C sp^2 covalent bond intensity in the α-CO_x resistive layer affects the forming voltage and the write and erase endurance cycle of the α-CO_x-based ReRAM cells. The result shows that a lower proportion of conductive C—C sp^2 covalent bond leads to longer write and erase endurance cycles.

1. Introduction

Recently, 3D cross-point memories have been extensively studied to open a new memory area that covers memory characteristics between the NAND-flash memory and dynamic random-access memory (DRAM).[1,2] Two types of 3D cross-point memories have been properly documented, including the storage-mapped memory using phase change random-access memory (PCRAM)[3–5] or resistive random-access memory (ReRAM)[6–10] and memory mapped memory using p-spin torque transfer random-access memory (p-STT-MRAM).[11,12] In addition, ReRAM or conductive bridge random-access memory (CBRAM)-based neurons and synapses[13–21] have been extensively studied for artificial neural networks in contrast with the complementary metal oxide semiconductor field effect transistor-based neurons and synapses that have a limited ability to achieve a higher neural density.[22–25] Moreover, all memories have nonvolatile memory characteristics unlike DRAM. The binary metal oxide-based ReRAM and CBRAM have a bi-stable resistance via electroforming or a rupture of oxygen vacancy filaments or metal ion filaments in the resistive layer in contrast with p-STTMRAM, which generates a bi-stable resistance state via spin-electron torque transfer and PCRAM producing bi-stable resistance states via phase change between amorphous and crystalline structures. On the other hand, an oxygenated amorphous carbon (α-CO_x)-based ReRAM has been recently reported, which presented a different bi-stable resistance generation mechanism via electroforming or a rupture of the conductive C—C sp^2 covalent bond filaments for achieving nonvolatile memory characteristics.[26] However, the bi-stable resistance by which such mechanism was generated was not yet proven. In particular, a precise correlation between the chemical bond depth profile (i.e., relative chemical bond intensities for conductive C—C sp^2 and insulating C—C sp^3 covalent bonds) in the α-CO_x resistive layer and an applied bias condition (i.e., a write or erase process) were not conducted.

Thus, in our study, α-CO_x-based ReRAM cells with a large memory-cell size (i.e., 60×60 μm^2 in memory-cell area) were specially designed to investigate the distribution of oxygen ions (O^{2-}) via electron energy loss spectroscopy (EELS) and chemical bond depth profiles using X-ray photoelectron spectroscopy (XPS) in the α-CO_x resistive layer, which were conducted just

S. M. Jin, H. J. Kim, D. S. Woo, S. M. Jung, J. G. Park
Department of Nano-scale Semiconductor Engineering
Hanyang University
Seoul 04763, Republic of Korea
E-mail: parkjgL@hanyang.ac.kr
D. E. Kim, J. G. Park
Department of Electronic Engineering
Hanyang University
Seoul 04763, Republic of Korea
T. H. Shim, J. G. Park
Advanced Semiconductor Materials and Devices Development Center
Hanyang University
Seoul 04763, Republic of Korea

The ORCID identification number(s) for the author(s) of this article can be found under https://doi.org/10.1002/aelm.202101083.

© 2022 The Authors. Advanced Electronic Materials published by Wiley-VCH GmbH. This is an open access article under the terms of the Creative Commons Attribution License, which permits use, distribution and reproduction in any medium, provided the original work is properly cited.

DOI: 10.1002/aelm.202101083

 © 2022 The Authors. Advanced Electronic Materials published by Wiley-VCH GmbH

after a write or an erase process. In particular, the dependencies of the O^{2-} distribution and the chemical bond depth profile on a set (i.e., write) or reset (i.e., erase) were investigated in detail to determine the exact bi-stable resistance generation mechanism of the α-CO_x ReRAM cells. In addition, the difference in the bi-stable resistance generation mechanism between a binary metal oxide-based ReRAM, CBRAM, and α-CO_x-based ReRAM was reviewed by empirically observing nonvolatile memory characteristics. Moreover, the dependency of the reliability (i.e., write and erase endurance cycles) on the intensity of the conductive C—C sp^2 covalent bonds in the α-CO_x resistive layer for the α-CO_x-based ReRAM-cells was examined by varying the partial pressures of the oxygen during sputtering of the α-CO_x resistive layer.

2. Results and Discussion

2.1. Bi-Stable Resistance Generation Mechanism Difference between Binary Metal Oxide-Based ReRAM, CBRAM, and α-CO_x-Based ReRAM

Three types of nonvolatile memories, such as binary metal oxide-based ReRAM, CBRAM, and α-CO_x-based ReRAM were fabricated, where the bottom W electrodes were used for all nonvolatile memories with a diameter of 60 nm to find and eliminate bi-stable resistance generation mechanism differences by the chemical reaction at the bottom electrodes, as shown in **Figure 1**a–c. The electroforming process is essential for producing oxygen vacancy filaments in the binary metal oxide-based ReRAM.[27–36] The bottom electrode has been used by a reactive electrode (e.g., W or Al), while the top electrode has been utilized by an inert electrode (e.g., Pt or TiN). On the other hand, the negatively charged oxygen ions (i.e., O^{2-}) in a binary metal oxide (i.e., HfO_x) resistive layer drifted and diffused from the top inert electrode (i.e., Pt) to the bottom reactive electrode (i.e., W) when a negative bias was applied to the inert top electrode (i.e., Pt), resulting in the production of oxygen vacancy (V_o^{2+}) filaments. Moreover, the current increased rapidly above forming voltage ($V_{forming}$), as shown by the pink line **a** of the voltage scanning from 0 to −1.60 V ($V_{forming}$) in Figure 1a and the left figure of Figure 1d. This process is called the electroforming process. Note that the electroforming of oxygen vacancy filaments in a resistive layer occurs locally on the bottom reactive electrode with a high electric field, as shown in **a**, **b**, and **c** of Figure S1b in the Supporting Information. The oxygen vacancy filaments would be ruptured near the bottom W electrode after an erase (reset) process, as shown by the yellow line **b** of the voltage scanning from 0 to 1.60 V reset voltage (V_{reset}) in Figure 1a and the right figure of Figure 1d. As a result, the read voltage (V_{read}) recognizes a high-resistance state (HRS). Otherwise, the oxygen vacancy filaments would be electroformed again from near the bottom electrode when a negative bias was applied resulting in

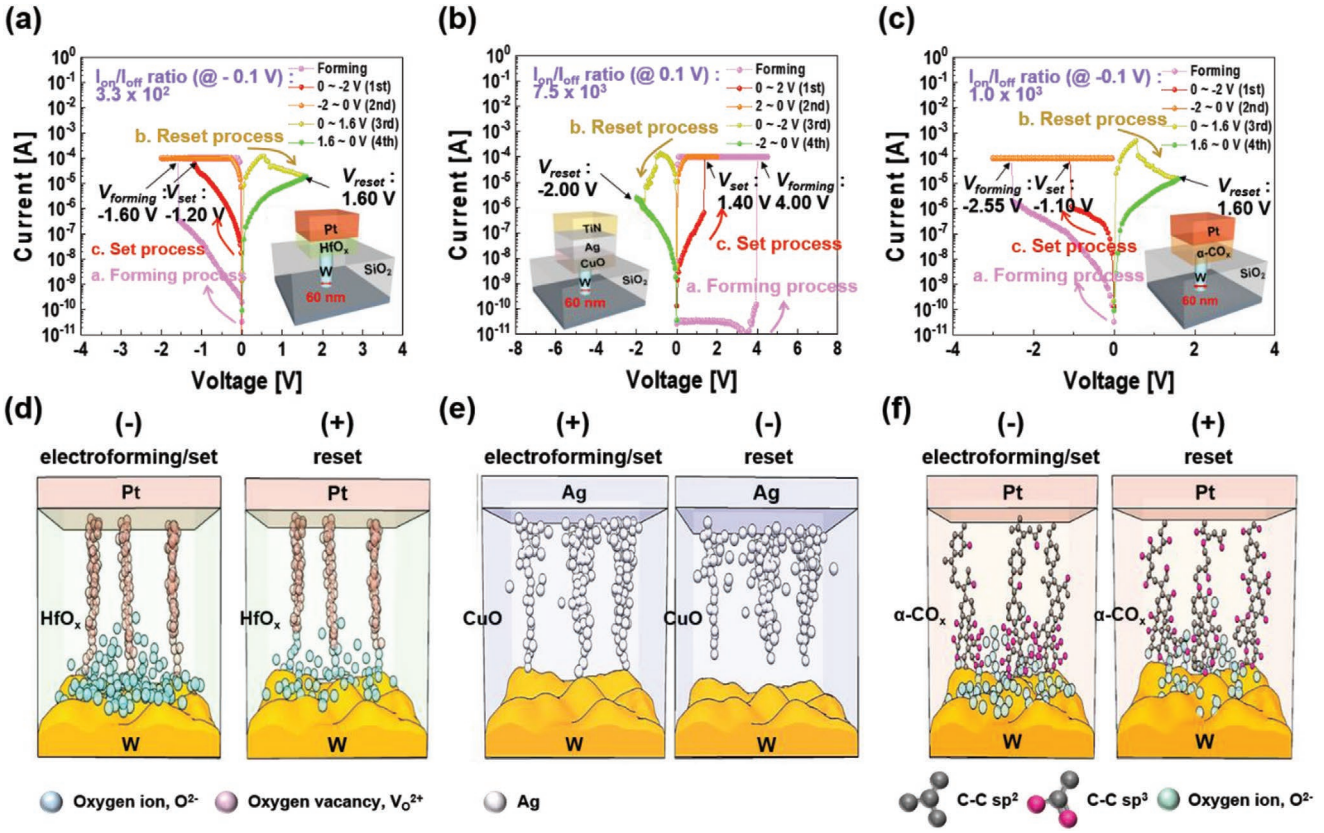

Figure 1. Comparison of the bi-stable resistance generation mechanism between binary metal oxide-based ReRAM, CBRAM, and α-CO_x-based ReRAM. Nonvolatile memory characteristics for a) binary metal oxide-based ReRAM, b) CBRAM, and c) α-CO_x-based ReRAM. Schematic of the electroforming, set, and reset for d) binary metal oxide-based ReRAM, e) CBRAM, and f) α-CO_x-based ReRAM.

© 2022 The Authors. Advanced Electronic Materials published by Wiley-VCH GmbH

V_{read} finding a low-resistance state (LRS), as shown by the red line **c** of the voltage scanning from 0 to –1.20 V set voltage (V_{set}) in Figure 1a and the left figure of Figure 1d. Therefore, a binary metal oxide-based ReRAM can produce a bi-stable resistance state through a set followed by a read (i.e., LRS) and a reset by a read (i.e., HRS). Note that oxygen vacancy filaments in a binary metal oxide resistive layer are produced when O^{2-} drift and diffuse toward the reactive electrode (i.e., W) during the set process rather than an inert electrode (i.e., Pt).[37–39]

Moreover, the generation mechanism of a bi-stable resistance for CBRAM was reported to be different from that of binary metal oxide-based ReRAM. An electroforming process produced metal ion filaments in a crystalline resistive layer (i.e., CuO) for CBRAM when a positive bias was applied on the top metal ion supplying electrode (i.e., Ag) and an inert electrode W since the positively charged Ag ions (Ag^+) drifted and diffused through the negatively charged metal vacancies (i.e., V_{Cu}^{2-}), as shown by the pink line **a** of the voltage scanning from 0 to 4.00 V ($V_{forming}$) in Figure 1b and the left figure of Figure 1e. The Ag^+ filaments with an inverse conical shape were electroformed in the resistive layer.[40] Moreover, Ag^+ filaments in the resistive layer near the bottom W electrode were ruptured after the electroforming and reset processes because Ag^+ located near the bottom electrode (i.e., W) diffused back to the resistive layer, as shown by the yellow line **b** of the voltage scanning from 0 to –2.00 V (V_{reset}) in Figure 1b and the right figure of Figure 1e. After a reset process, the CBRAM presented an HRS when a positive V_{read} that was less than V_{set} was applied to the top electrode. On the other hand, Ag^+ filaments in the resistive layer were electroformed again when a positive bias was applied to the top Ag electrode, which was called a set process. Therefore, the CBRAM exhibited an LRS when a positive read voltage was applied to the top Ag electrode, as shown by the red line **c** of the voltage scanning from 0 to 1.40 V (V_{set}) in Figure 1b and the left figure of Figure 1e. A bi-stable resistance of CBRAM was obtained by electroforming or a rupture of metal ion filaments in the resistive layer.[41–44]

Finally, oxygenated amorphous carbon-based (α-CO_x) ReRAM presents a different bi-stable resistance generation mechanism, which was different from binary metal oxide-based ReRAM and CBRAM.[45,46] It utilizes an α-CO_x resistive layer containing both insulating C—C sp^3 and conductive C—C sp^2 covalent bonds. Electroforming can produce conductive C—C sp^2 covalent bonds in the α-CO_x resistive layer because the negatively charged O^{2-} drifted and diffused from the top inert electrode (e.g., Pt) to the bottom reactive electrode (e.g., W) when a negative bias was applied to the top inert (e.g., Pt). Therefore, the amount of conductive C—C sp^2 covalent bonds was enhanced, while that of insulating C—C sp^3 covalent bonds was considerably reduced. This process is called an electroforming process of the conductive C—C sp^2 covalent bond filaments in the resistive layer, as shown by the pink line **a** of the voltage scanning from 0 to –2.55 V ($V_{forming}$) in Figure 1c and the left figure of Figure 1f. The negatively charged O^{2-} drifted and diffused back from the bottom W electrode to the top Pt electrode when a positive bias was applied to the top inert electrode. As a result, the amount of conductive C—C sp^2 covalent bonds near the top electrode was reduced, while that of insulating C—C sp^3 covalent bonds was enhanced. This resulted in the rupture of the conductive C—C sp^2 covalent bond filaments near the top electrode, called the reset process. A negative V_{read}, which is less than V_{set}, revealed an HRS after the reset process, as shown by the yellow line **b** of the voltage scanning from 0 to 1.60 V (V_{reset}) in Figure 1c and the right figure of Figure 1f. On the other hand, the negatively charged O^{2-} drifted and diffused back again from the top Pt electrode to the bottom W electrode when a negative bias was applied to the top inert electrode. As a result, the conductive C—C sp^2 covalent bonds near the top electrode of the α-CO_x resistive layer increased. This process is called a set process. A negative V_{read} detected an LRS after the set process, as shown by the red line **c** of the voltage scanning from 0 to –1.10 V (V_{set}) in Figure 1c and the left figure of Figure 1f. Based on the review of the bi-stable resistance generation mechanism, the stable resistance state of the α-CO_x-based ReRAM was originated via electroforming or a rupture of the conductive C—C sp^2 covalent bond filaments near the top electrode of the α-CO_x resistive layer, while the stable resistance state of the binary metal oxide-based ReRAM and CBRAM was originated via electroforming or rupture of oxygen vacancy filaments (V_O^{2+}) and metal ion filaments near the bottom electrode of a resistive layer.

2.2. Bi-Stable Resistance Generation Mechanism for α-CO_x-Based ReRAM

An intentional α-CO_x-based ReRAM cell with a large cell area (i.e., 60 × 60 μm^2) and an oxygen partial-pressure of 10.7% during sputtering of the resistive layer were fabricated, as shown in **Figure 2**a. The chemical composition (i.e., Pt, C, O, and W) depth profiles of the α-CO_x resistive layer were performed via energy dispersive X-ray spectroscopy (EDS) and EELS, to investigate the mechanism by which a bi-stable resistance for the α-CO_x-based ReRAM was generated. The current–voltage (I–V) curve presented the bi-stable resistance (i.e., I_{on}/I_{off} of ≈1.25×10^1) at $V_{forming}$ of –1.10 V, V_{reset} of 1.00 V, and V_{set} of –0.60 V, as shown in Figure 2b. In particular, it was confirmed that the photolithography process of the memory-cell array did not induce the surface etching damage of the α-CO_x resistive switching layer, as shown in Figure S2 in the Supporting Information. In addition, the detailed current conduction mechanisms for electroforming, set, and reset process were reviewed by I–V curves fitting with dominant current conduction mechanism, as shown in Figure S3 in the Supporting Information. Electroforming and set process followed space-charge-limited-conduction. The LRS followed Ohmic conduction due to the formation of C—C sp^2 covalent bonding filament in α-CO_x resistive switching layer. The negative-differential-resistance (i.e., reset process) followed Poole–Frenkel conduction due to the formation of C—C sp^3 covalent bonding in the α-CO_x resistive switching layer. A cross-sectional transmission electron microscopy (TEM) image was obtained to examine the crystalline structure of the α-CO_x resistive layer in the pristine state, indicating that the α-CO_x resistive layer had an amorphous structure and the Pt and W had a polycrystalline structure, as shown in Figure 2c. Note that the α-CO_x resistive layer with a thickness of ≈20 nm showed an amorphous structure, which was confirmed by X-ray diffraction (XRD), as shown in Figure S4 in the Supporting Information. The chemical composition (i.e., C and O^{2-}) depth profiles in the α-CO_x resistive layer

© 2022 The Authors. Advanced Electronic Materials published by Wiley-VCH GmbH

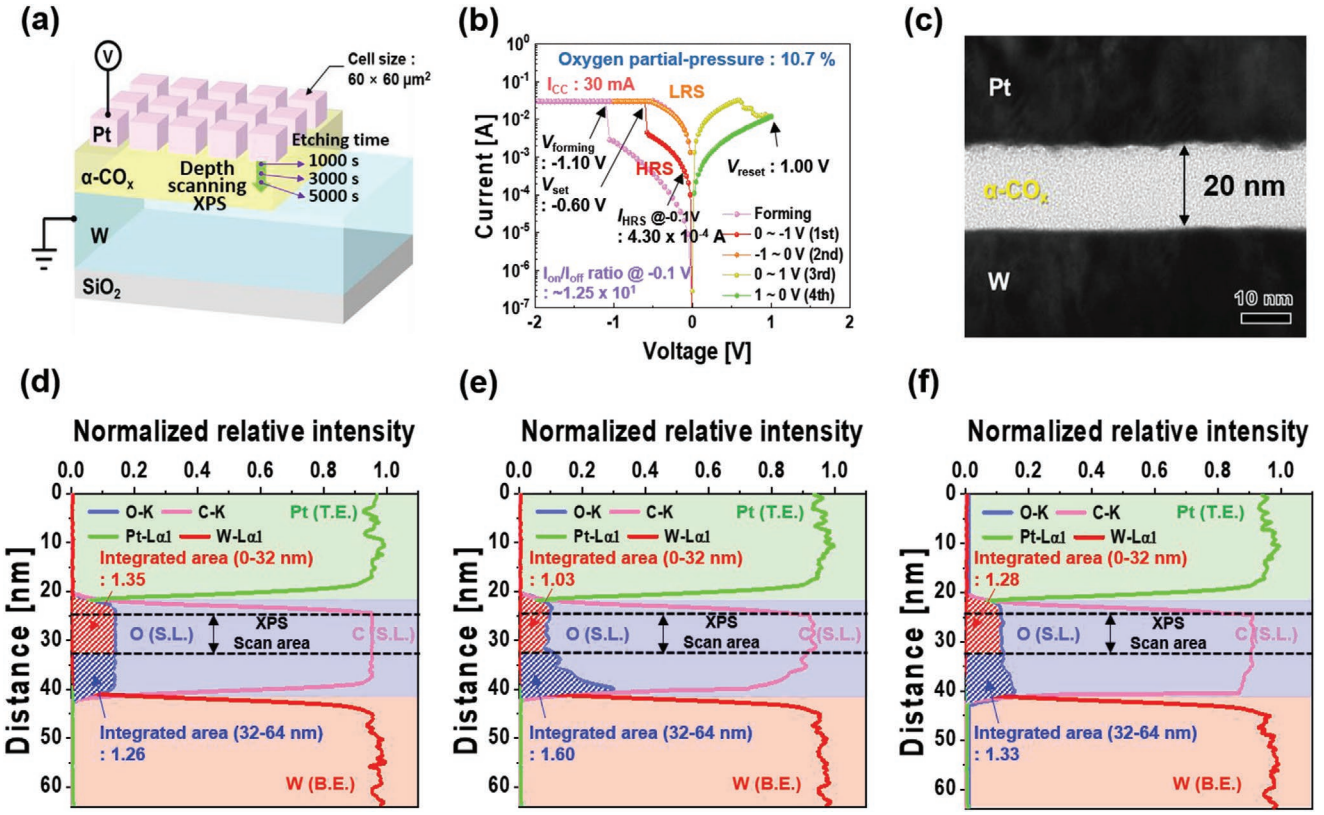

Figure 2. Dependency of O^{2-} ions distribution on pristine, set, and reset. a) Schematic of the α-CO_x-based ReRAM cell with an area of 60 × 60 μm^2. b) Nonvolatile memory characteristics. c) Cross-sectional TEM image of the memory cell. Chemical composition (i.e., O, C, Pt, and W) depth profiles d) at the pristine state, e) after the set process, and f) after the reset process using EDS and EELS. Normalized relative chemical composition intensity was obtained by averaging the intensities of the lateral 100 pixels.

were analyzed as a function of the pristine state after a set process and after a reset process using EDS and EELS elemental mapping, as shown in Figure S5a–c in the Supporting Information. In the pristine state, C and O atoms were uniformly distributed in the α-CO_x resistive layer. Here, the integrated area of the relative O^{2-} intensity (i.e., concentration) from the top Pt electrode to half the thickness of the α-CO_x-based ReRAM-cell (i.e., 0–32 nm in depth) was 1.35 arbitrary unit (a.u.), while that from a half-thickness of α-CO_x-based ReRAM cell to bottom W electrode (i.e., 32–64 nm in depth) was 1.26 a. u., as shown in Figure 2d. The relative intensity of O^{2-} in the α-CO_x resistive layer after the set process increased with the depth of the resistive layer. Specifically, O^{2-} near the bottom W electrode were piled up as they drifted and diffused from the top Pt electrode to the bottom W electrode when a negative bias was applied to the top Pt electrode, as shown in Figure 2e. In addition, the relative C atomic intensity was sustained uniformly from the Pt top electrode to the two-third depth of the α-CO_x resistive layer and then rapidly reduced toward the bottom W electrode. Moreover, the integrated area of the relative O^{2-} intensity from the top Pt electrode to a half-depth of α-CO_x-based ReRAM cell (i.e., 0–32 nm in depth) after a set process (i.e., 1.03 a.u.) was reduced considerably compared to that for a pristine state (i.e., 1.35 a.u.). Otherwise, the integrated area of the relative O^{2-} intensity from a half-depth of α-CO_x-based ReRAM cell to the bottom W electrode (i.e., 32–64 nm in depth) after a set process (i.e., 1.60 a.u.) was enhanced compared to that for a pristine state (i.e., 1.26 a.u.), indicating that O^{2-} covalently bonded with C atoms drifted and diffused toward the bottom W electrode when a negative bias was applied to the top Pt electrode. As a result, the covalent bond states of C atoms in the α-CO_x resistive layer between the top Pt electrode and a half-depth of the resistive layer would be changed, which will be proven later. Moreover, the integrated area of the relative O^{2-} intensity from the top Pt electrode to a half-depth of α-CO_x-based ReRAM cell (i.e., 0–32 nm in depth) after the reset process (i.e., 1.28 a.u.) was increased after the set process (i.e., 1.03 a.u.). Meanwhile, that from a half-depth of α-CO_x-based ReRAM cell to the bottom W electrode (i.e., 32–64 nm in depth) for an after a reset process (i.e., 1.33 a.u.) was decreased than that after a set process (i.e., 1.60 a.u.), as shown in Figure 2f. In addition, the relative C atomic intensity close to the bottom W electrode after a reset process was increased back. These results imply that O^{2-} ions covalently bonded with C atoms that drifted and diffused back toward the top Pt electrode when a positive bias was applied to the top Pt electrode, and the covalent bond states of C atoms in the α-CO_x resistive layer would vary. Therefore, the dependencies of the relative C and O^{2-} intensities on the bias conditions demonstrate that the generation of a bi-stable resistance in Figure 2b was correlated with the distribution of the relative C and O^{2-} intensities in the α-CO_x resistive layer by comparing Figure 2d with Figure 2e,f, indicating that O^{2-}

© 2022 The Authors. Advanced Electronic Materials published by Wiley-VCH GmbH

drifted and diffused based on the bias conditions to ensure that the covalent bond states of C would be transformed based on the bias conditions.

In order to investigate detailed C—C covalent bond composition of the α-CO_x-based resistive switching layer, the carbon K-edge EELS spectrum of the α-CO_x-based resistive switching layer as a function of pristine, after the set process, and after the reset process was examined, as shown in **Figure 3**. The cross-sectional scanning transmission electron microscopy (STEM) image of the α-CO_x-based ReRAM-cell was presented, as shown in Figure 3a. The carbon K-edge EELS spectrum was extracted over the entire region of the α-CO_x-based resistive switching layer. In the pristine state, the integrated area of π^* peak and σ^* peak intensity were 3.18 and 18.75, respectively, as shown in Figure 3b. After a set process, the integrated area of π^* peak and σ^* peak intensity were 3.62 and 16.14, respectively, as shown in Figure 3c. Otherwise, after a reset process, the integrated area of π^* peak and σ^* peak intensity were 3.22 and 18.04, respectively, as shown in Figure 3d. Based on the calculation of the fraction of C—C sp^2 covalent bond developed by Berger et al.,[47,48] the fraction of C—C sp^2 covalent bond for the pristine state, after the set process, and after the reset process, was ≈55.6, ≈73.6, and ≈58.5%, respectively. Highly oriented pyrolytic graphite was used as a reference. These results indicate that the pristine state, after the set process, or after the reset process of the α-CO_x-based ReRAM cell was dominantly determined by the fraction magnitude of C—C sp^2 covalent bond in the α-CO_x-based resistive switching layer.

The dependence of the chemical bond depth profiles on the bias conditions was investigated via depth scanning XPS using the gas-cluster-ion-source (GCIS) with accelerating voltage of 4 KeV and cluster size of 2000 to determine how the O^{2-} distribution depends on after a set process or after a reset process influences the covalent-bond states of C atoms in the α-CO_x resistive layer. At the α-CO_x-based ReRAM cells having an area of 60 × 60 μm^2, as shown in Figure 2a, with a pristine state, after the set and reset processes, the top Pt electrodes were etched off by the GCIS (i.e., Ar_n^+ cluster) for ion milling in XPS. Subsequently, the α-CO_x resistive layers were etched up to near the top Pt electrode (i.e., the α-CO_x resistive layer with a thickness of ≈4 nm: etching time of 1000 s) at one-fourth depth of the α-CO_x resistive layer (i.e., depth of 8 nm: etching time of 3000 s), and at a half-depth of the α-CO_x resistive layer (i.e., depth of 12 nm: etching time of 5000 s). Therefore, chemical bonds were observed at the three locations using XPS. The XPS peak signals of C—C sp^2 (conductive C covalent bond), C—C sp^3 (insulating C covalent bond), C=O (carbonyl), O—C=O (carboxyl), and O—(C=O)—O (carbonate) were found at 284.4, 285.2, 286.4, 287.7, and 289.1 eV, respectively.[49,50] First, the integrated area of C—C sp^2, C—C sp^3, C=O, O—C=O, and O—(C=O)—O near the top Pt electrode in the pristine state was 5278, 5166, 1717, 791, and 433, respectively, indicating that

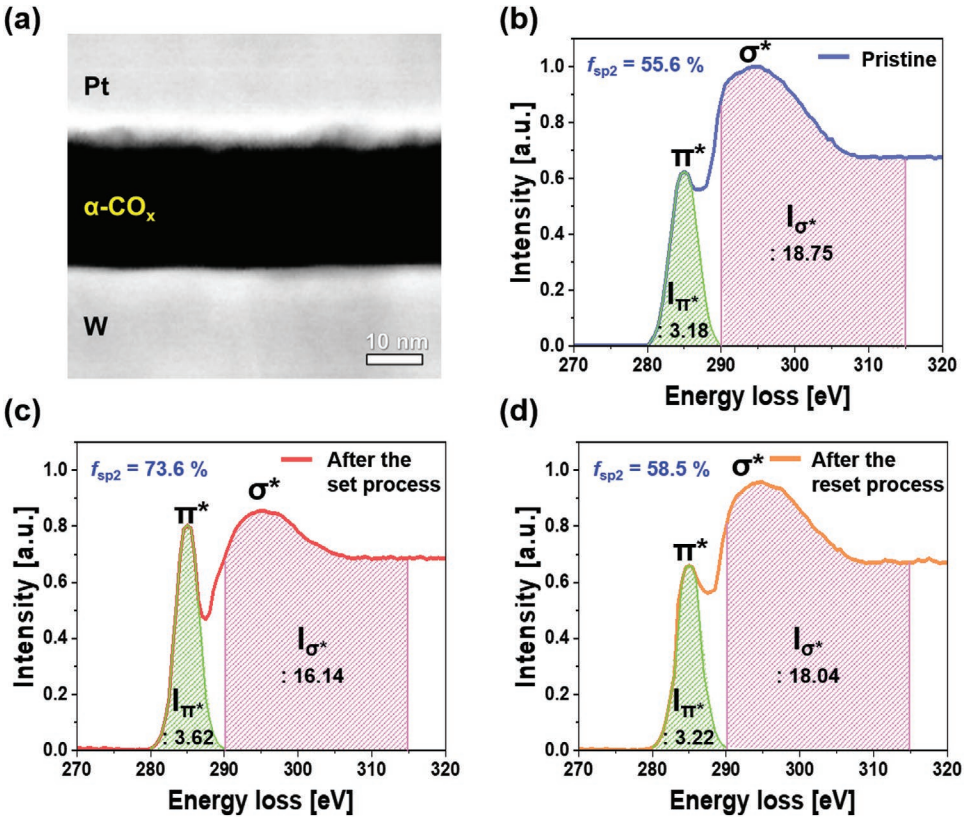

Figure 3. Dependency of the fraction magnitude of C—C sp^2 covalent bond on pristine, after the set process, or after the reset process for the α-CO_x-based ReRAM-cell. a) Cross-sectional scanning transmission electron microscopy (STEM) image of the α-CO_x-based ReRAM-cell. The carbon K-edge EELS spectrum was extracted over the entire region of the α-CO_x-based resistive switching layer. The carbon K-edge EELS spectrum of the α-CO_x-based ReRAM-cell b) in the pristine state, c) after the set process, and d) after the reset process.

 © 2022 The Authors. Advanced Electronic Materials published by Wiley-VCH GmbH

the integrated area percentages of C—C sp^2, C—C sp^3, C=O, O—C=O, and O—(C=O)—O covalent bonds in the α-CO_x resistive layer were 39.5%, 38.6%, 12.8%, 5.9%, and 3.2%, as shown in **Figure 4**a and Figure S6a in the Supporting Information. In particular, the integrated area percentage of the C—C sp^2 bond (i.e., 39.5%) in the α-CO_x resistive layer was almost similar to that of the C—C sp^3 bond (i.e., 38.6%), indicating that the α-CO_x resistive layer in the pristine state would be an insulating resistive layer. In addition, the XPS intensities for all covalent bonds at the one-fourth and half-depths of the α-CO_x resistive layer in the pristine state were almost similar to those near the Pt top electrode, as shown in Figure 4a–c and Figure S6a–c in the Supporting Information, which are well correlated with Figure 2d. Second, the integrated areas of C—C sp^2, C—C sp^3, C=O, O—C=O, and O—(C=O)—O near the top Pt electrode after a set process were 7927, 1859, 1191, 457, and 266, showing that the integrated area percentages of C—C sp^2, C—C sp^3, C=O, O—C=O, and O—(C=O)—O were 67.7%, 15.9%, 10.2%, 3.9%, and 2.3%, respectively, as shown in Figure 4d and Figure S6d in the Supporting Information. The integrated area percentage of the C—C sp^2 bond was enhanced from 39.5% to 67.7%, while those of the C—C sp^3, C=O, O—C=O, and O—(C=O)—O covalent bonds were reduced from 38.6% to 15.9%, 12.8% to 10.2%, 5.9% to 3.9%, and 3.2% to 2.3%, respectively. In particular, the integrated area percentage of the C—C sp^2 bond was increased by ≈28.2%, while that of the C—C sp^3 bond was decreased by ≈22.7%, indicating that after a set process of the α-CO_x-based ReRAM cell enhances the conductive C—C sp^2 covalent bonds and reduces the insulating C—C sp^3 covalent bonds in the α-CO_x resistive layer. As a result, conductive C—C sp^2 covalent bond filaments were produced near the top electrode of the α-CO_x resistive layer. The integrated area

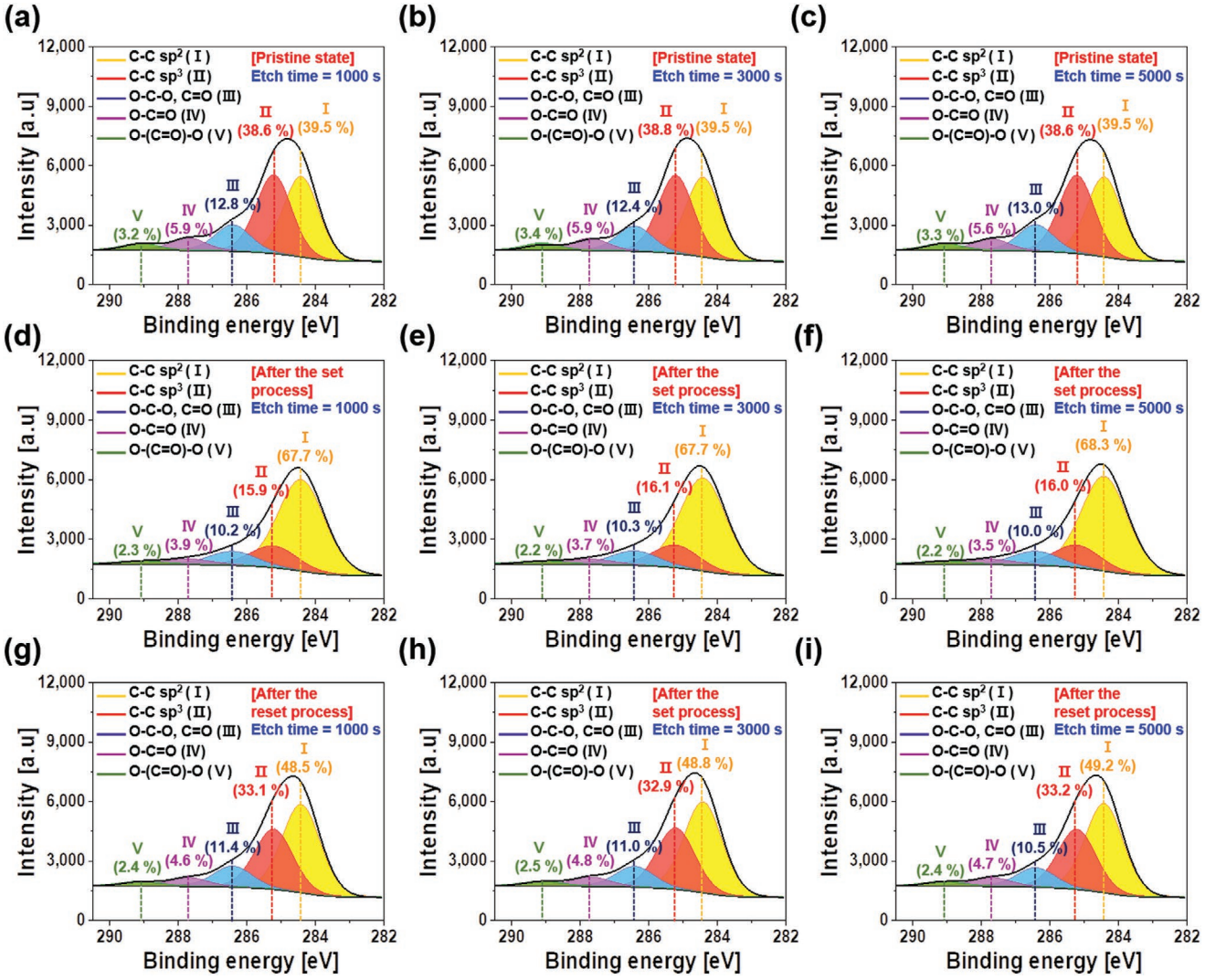

Figure 4. Dependency of chemical bond depth-profiles on pristine, set, and reset for α-CO_x-based ReRAM-cells, analyzed by depth scanning XPS using the gas cluster ion source (GCIS). The chemical bond intensities for C—C sp^2 (conductive C covalent bond), C—C sp^3 (insulating C covalent bond), C=O (carbonyl), O—C=O (carboxyl), and O—(C=O)—O (carbonate) for a pristine state located a) from top electrode to a depth of 4 nm, b) depth of ≈4–8 nm, and c) depth in the α-CO_x resistive layer of ≈8–12 nm. Result after the set process located d) from top electrode to a depth of 4 nm, e) depth of ≈4–8 nm, and f) depth in the α-CO_x resistive layer of ≈8–12 nm. Those for after the reset process located g) from top electrode to a depth of 4 nm, h) depth of ≈4–8 nm, and i) depth in the α-CO_x resistive layer of ≈8–12 nm.

© 2022 The Authors. Advanced Electronic Materials published by Wiley-VCH GmbH

percentages of all covalent bonds near the top Pt electrode after the set process were almost similar to those of the one-fourth and half-depth of the α-CO_x resistive layer since the O^{2-} intensity was uniformly distributed between the near top Pt electrode and half-depth of the α-CO_x resistive layer, as shown in Figures 2e and 4d–f. Note that O^{2-} drifted and diffused from the top Pt electrode to the bottom W electrode after a set process to ensure that the relative intensity of O^{2-} near the top Pt electrode was considerably reduced, as shown in Figure 2d,e. Therefore, the conductive C—C sp^2 covalent bonds in the α-CO_x resistive layer near the top Pt electrode after the set process were significantly increased, while the insulating C—C sp^3 covalent bonds were considerably decreased. In addition, the presence of a covalent O atom with C—C covalent bonds determines the insulating C—C sp^3 and conductive C—C sp^2 covalent bonds in the α-CO_x resistive layer. Finally, the integrated areas of C—C sp^2, C—C sp^3, C=O, O—C=O, and O—(C=O)—O near the top Pt electrode after the reset process were 6269, 4283, 1480, 596, and 304, respectively, indicating that the integrated area percentages of C—C sp^2, C—C sp^3, C=O, O—C=O, and O—(C=O)—O were 48.5%, 33.1%, 11.4%, 4.6%, and 2.4%, as shown in Figure 4g and Figure S6g in the Supporting Information. The integrated area percentage of the C—C sp^2 bond decreased from 67.7% to 48.5%, while those of the C—C sp^3, C=O, O—C=O, and O—(C=O)—O covalent bonds increased from 15.9% to 33.1%, 10.2% to 11.4%, 3.9% to 4.6%, and 2.3% to 2.4%, respectively. In particular, the integrated area percentage of the C—C sp^2 bond was decreased by ≈19.2%, while that of the C—C sp^3 bond was increased by ≈17.2%. This implies that after a reset process of the α-CO_x-based ReRAM cell significantly reduces the conductive C—C sp^2 covalent bonds and increases the insulating C—C sp^3 covalent bonds in the α-CO_x resistive layer. The integrated area percentages of all covalent bonds near the top Pt electrode of the set process were similar to those of the one-fourth and half-depth of the α-CO_x resistive layer because the O^{2-} intensity was uniformly distributed between the near-top Pt electrode and half-depth of the α-CO_x resistive layer, as shown in Figures 2f and 4g–i. A reset process performed the drift and diffusion of O^{2-} from the bottom W electrode back to the top Pt electrode so that the relative intensity of O^{2-} between the Pt electrode and half-depth of the α-CO_x resistive layer was considerably increased, as shown in Figure 2e,f. As a result, the conductive C—C sp^2 covalent bonds in the α-CO_x resistive layer were decreased while the insulating C—C sp^3 covalent-bonds were increased near the top electrode of the α-CO_x resistive layer, called a reset process. In summary, the dependency of the C—C sp^2 or C—C sp^3 covalent bond integrated area percentages on a set or reset evidently proved a considerable transformation from the insulating C—C sp^3 covalent bonds to the conductive C—C sp^2 covalent bonds during the set process in the α-CO_x resistive layer near the top Pt electrode, accomplishing an LRS, while a significant transformation from the conductive C—C sp^2 covalent bonds to the insulating C—C sp^3 covalent bonds during the reset process ruptured the conductive C—C sp^2 filaments in the α-CO_x resistive layer near the top Pt electrode, achieving an HRS, as shown in Figure S7a–c in the Supporting Information. Therefore, the correlation between the chemical bond intensities and an applied bias condition via simultaneous EDS, EELS, and XPS analysis proved that a bi-stable resistance generation mechanism for the α-CO_x-based ReRAM was different from those for binary metal oxide-based ReRAM and CBRAM.

2.3. Dependencies of Nonvolatile Memory Characteristics on the Conductive C—C sp^2 Covalent Bond Intensity for α-CO_x-Based ReRAM

The dependencies of nonvolatile memory characteristics on the chemical composition were observed as a function of the chemical composition intensities because the O^{2-} intensity in the α-CO_x resistive layer near the bottom W electrode determined the bi-stable resistance of the α-CO_x-based ReRAM cells. The chemical composition of the α-CO_x resistive layer was varied by controlling the partial pressures of the oxygen (i.e., 0%, 3.8%, 7.4%, 10.7%, and 13.8%) during sputtering of the α-CO_x resistive layer. Then, the nonvolatile memory characteristics were estimated and correlated with the chemical bond of the α-CO_x resistive films sputtered with five different partial pressures of the oxygen for all α-CO_x-based ReRAM cells. Moreover, memory cells with a diameter of 60 nm were fabricated for commercial memory applications, as shown in **Figure 5**a. The values for $V_{forming}$, V_{reset}, V_{set}, and memory margin (I_{on}/I_{off}) were –1.80, 1.60, –1.05, and ≈3.6×10^2, respectively, for α-CO_x-based ReRAM cells without oxygen flow during sputtering. This demonstrates a typical bi-stable resistance, as shown in Figure 5b. Otherwise, $V_{forming}$ increased linearly from –1.80, –2.00, –2.20, and –2.55 V, V_{reset} and V_{set} were sustained at ≈1.60 and –1.05 to –1.10 V, and memory margin (I_{on}/I_{off}) increased from ≈3.6×10^2, 4.3×10^2, 8.1×10^2, and 1.0×10^3, respectively, as shown in Figure 5b–e and inset of Figure 5f, for the α-CO_x- based ReRAM cells using the increased partial pressures of the oxygen during sputtering. In particular, the nonvolatile memory characteristics completely disappeared for the α-CO_x-based ReRAM cells using an oxygen partial pressure of 13.8% during sputtering because the α-CO_x resistive layer would be changed toward the insulating layer, as shown in Figure 5f. In addition, the dependency of reliability on the chemical composition determined by the partial pressure of the oxygen during sputtering was measured. The write and erase endurance cycle was 6.0×10^2 cycles and a set-stuck failure occurred for the α-CO_x-based ReRAM cells without oxygen flow during sputtering. Otherwise, the write and erase endurance cycle increased from 6.0×10^2, 2.0×10^4, 5.0×10^5, and $>1.0 \times 10^6$ cycles for the α-CO_x-based ReRAM cells when oxygen partial pressure increased from 0% to 3.8%, 7.4%, and 10.7%, as shown in Figure 5g–j,l. Note that the endurance cycle could not be measured for the partial pressure of 13.8% because the resistive layer would be a complete insulating layer, as shown in Figure 5k,l. Moreover, the dependency of the retention time on oxygen partial pressure for the α-CO_x-based ReRAM cells is shown in Figure S8 in the Supporting Information. The retention time for the α-CO_x-based ReRAM cells sputtered at oxygen partial pressure of 0%, 3.8%, 7.4%, and 10.7% was ≈5.3, ≈6.4, ≈7.6, and ≈8.6 years, indicating that the retention time increased with oxygen partial pressure. These results indicate that the nonvolatile memory characteristics of the α-CO_x-based ReRAM cells greatly depended on the chemical compositions determined by the partial pressure of

© 2022 The Authors. Advanced Electronic Materials published by Wiley-VCH GmbH

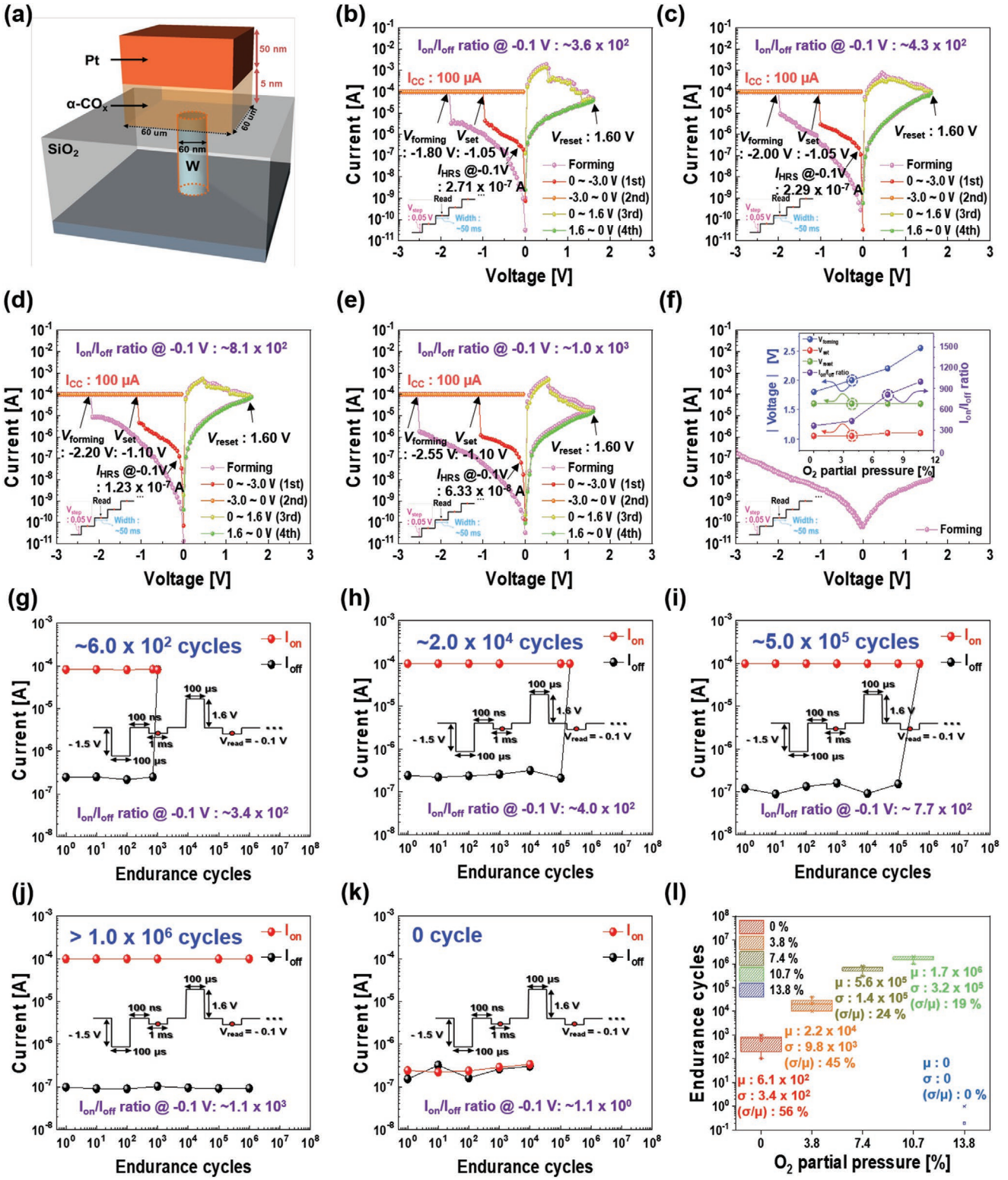

Figure 5. Dependency of nonvolatile memory characteristics and reliabilities (i.e., write and erase endurance cycle) on the chemical composition (i.e., conductive C—C sp^2 and insulating C—C sp^3 covalent bonds) determined by the partial pressure of the oxygen during sputtering the α-CO_x resistive layer for ReRAM cells. a) Schematic α-CO_x-based ReRAM cell with a diameter of 60 nm. Nonvolatile memory characteristics b) without oxygen flow, and with oxygen partial-pressure of c) 3.8%, d) 7.4%, e) 10.7%, and f) 13.8%. The inset of Figure 4f presents the dependencies of $V_{forming}$, V_{set}, V_{reset}, and I_{on}/I_{off} ratio on the partial pressure of the oxygen. Write and erase endurance cycles for g) without oxygen flow, and oxygen partial-pressure of h) 3.8%, i) 7.4%, j) 10.7%, and k) 13.8%. l) Statistical write and erase endurance depending on the partial pressure of the oxygen.

© 2022 The Authors. Advanced Electronic Materials published by Wiley-VCH GmbH

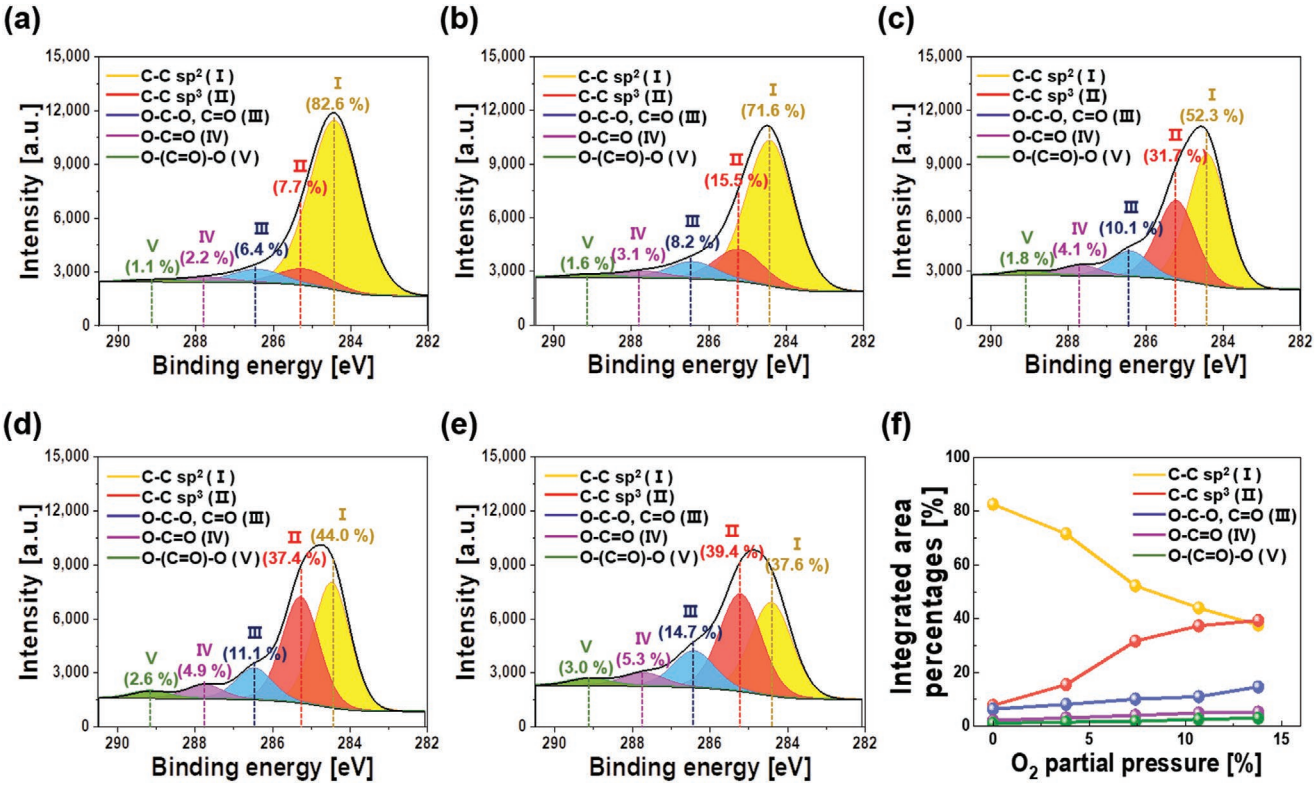

Figure 6. Chemical bond (i.e., C—C sp^2 (conductive C covalent bond), C—C sp^3 (insulating C covalent bond), C=O (carbonyl), O—C=O (carboxyl), and O—(C=O)—O (carbonate)) intensities depending on the partial pressure of the oxygen during sputtering the α-CO_x resistive layer. The chemical bond intensities for the α-CO_x resistive layer at a pristine state were measured at the surface of the resistive layer. Chemical bond intensities a) without oxygen flow, and oxygen partial-pressure of b) 3.8%, c) 7.4%, d) 10.7%, and e) 13.8%. f) Integrated area percentages depending on the partial pressure of the oxygen.

the oxygen during the resistive layer sputtering. This indicates that a higher partial pressure of the oxygen led to an improved nonvolatile memory characteristic and reliability. The detailed chemical bonds of the α-CO_x resistive films were characterized using XPS as a function of the partial pressure of the oxygen to correlate nonvolatile memory characteristics with the chemical bond. The integrated area percentages of the conductive C—C sp^2 covalent bond in the α-CO_x resistive layer decreased to 82.6%, 71.6%, 52.3%, 44.0%, and 37.6%, respectively, while those of the insulating C—C sp^3 covalent bonds were enhanced to 7.7%, 15.5%, 31.7%, 37.4%, and 39.4% when the oxygen partial pressure increased from 0%, 3.8%, 7.4%, 10.7%, and 13.8%, as shown in **Figure 6**a–f. In particular, the integrated area percentages of the covalent bonds C=O, O—C=O, and O—(C=O)—O in the α-CO_x resistive layer were increased as the partial pressure of the oxygen increased. It is evident from the comparison of Figure 5b–f with Figure 6a–e that as the oxygen partial pressure increased from 0%, 3.8%, 7.4%, and 10.7%, respectively, HRS (I_{off} at −0.1 V V_{read}) decreased from 2.71×10^{-7}, 2.29×10^{-7}, 1.23×10^{-7}, and 6.33×10^{-8} A, respectively. Furthermore, the integrated area percentages of the conductive C—C sp^2 covalent bonds decreased from 82.6%, 71.6%, 52.3%, 44.0%, and 37.6%, respectively, while those of the insulating C—C sp^3 covalent bonds increased from 7.7%, 15.5%, 31.7%, 37.4%, and 39.4%, respectively. Note that a lower integrated area percentage of the conductive C—C sp^2 covalent bonds shown through the comparison of Figure 5g–l with Figure 6a–f resulted in a longer write and erase endurance cycles of the α-CO_x-based ReRAM. Moreover, it was confirmed that the retention time of the α-CO_x-based ReRAM cells was ≈8.6 years at 85 °C, as shown in Figure S8d in the Supporting Information. The α-CO_x-based ReRAM cells presented a typical forming (i.e., ≈280 ns), set (i.e., ≈85 ns), and reset (i.e., ≈75 ns) speeds such as binary metal oxide-based ReRAM and CBRAM cells, as shown in Figure S9 in the Supporting Information.

3. Conclusion

Generally, the α-CO_x-based ReRAM cell have presented advantages compare to binary metal oxide-based ReRAM, since it can be produced by low cost due to a cheap graphite target and can ensure reliable nonvolatile memory characteristics due to superior resilience to external stimuli such as friction, heat, and shock.[46] In addition, as shown in Figure S10 in the Supporting Information, the α-CO_x-based ReRAM cell could demonstrate a better synaptic device performance than binary metal oxide-based ReRAM and CBRAM,[51–53] showing at least 32-level (i.e., 5-bit) conductance, where online learning of neuromorphic system is necessary at least 32-level (i.e., 5-bit) conductance.[54] Moreover, the α-CO_x ReRAM cells demonstrated a different bistable resistance mechanism than the binary metal oxide-based

© 2022 The Authors. Advanced Electronic Materials published by Wiley-VCH GmbH

ReRAM cells and CBRAM cells. In particular, the bi-stable resistance generation of the α-CO_x ReRAM cells was determined by the O^{2-} distribution near the bottom W electrode, depending on the applied bias polarity on the top electrode. The conductive C—C sp^2 covalent bond filaments were electroformed near the top Pt electrode when O^{2-} were accumulated near the bottom W electrode due to the diffusion and drift of the O^{2-} toward the bottom W electrode after applying a negative bias on the top Pt electrode. On the other hand, the conductive C—C sp^2 covalent bond filaments were ruptured near the top Pt electrode when O^{2-} drifted and diffused back toward the top Pt electrode after applying a positive bias. In addition, the intensity of conductive C—C sp^2 covalent bond in the α-CO_x resistive layer determined the forming voltage of the α-CO_x ReRAM cells, which was dependent on the partial pressure of the oxygen during the sputtering of the α-CO_x resistive layer. The proportion of conductive C—C sp^2 covalent bond decreased as the partial pressure of the oxygen increased during sputtering. Therefore, a lower proportion of conductive C—C sp^2 covalent bond led to a higher forming voltage. Subsequently, the set voltage or reset voltage was almost independent of the partial pressure of the oxygen during sputtering after forming the conductive C—C sp^2 covalent bond filaments in the α-CO_x resistive layer. Moreover, the conductive C—C sp^2 covalent bond intensity in the α-CO_x resistive layer affected the forming voltage and the write and erase endurance cycle of the α-CO_x ReRAM cells. A less proportion of conductive C—C sp^2 covalent bond led to longer write and erase endurance cycles. However, a bi-stable resistance was not produced at less than a specific proportion of conductive C—C sp^2 covalent bond in the pristine state (i.e., the integrated area percentage of ≈37.6%). Furthermore, LRS and HRS depended on the operating temperature of memory cells, indicating that the resistance of both LRS and HRS decreased as the temperature increased and the slope of HRS decreased more than that of LRS, which was similar to binary metal oxide-based ReRAM[55–57] and different from CBRAM cell,[58–60] as shown in Figure S11 in the Supporting Information. Note that the resistance of both HRS and LRS for α-CO_x-based ReRAM and binary metal oxide-based ReRAM decreased as the operating temperature increased. Otherwise, the resistance of LRS for CBRAM increased as the operating temperature increased. Finally, the α-CO_x ReRAM cells fundamentally require a relatively high forming voltage of conductive C—C sp^2 covalent bond filaments. Therefore, further studies are necessary to achieve forming-free in commercial α-CO_x ReRAM cells and understand the mechanism by which the intensity of the conductive C—C sp^2 covalent bonds in the α-CO_x resistive layer influences the memory characteristics and reliability. In addition, a novel study that focuses on a memristor-type synapse using α-CO_x ReRAM cells and integrate-and-fire neurons using the negative-differential-resistance (NDR) of the α-CO_x ReRAM cells is necessary.

4. Experimental Section

Fabrication of Nanoscale Binary Metal Oxide-Based ReRAM Cells, CBRAM, and α-CO_x-Based ReRAM Cells: Three types of nanoscale nonvolatile memory cells with a bottom electrode (diameter of ≈60 nm), such as binary metal oxide-based ReRAM cells, CBRAM, and α-CO_x-based ReRAM cells, were fabricated. A SiO_2 film with a thickness of ≈30 nm was deposited on a 12 in. SiO_2 wafer by chemical vapor deposition, and nanoholes with electrodes (diameter of ≈60 nm) were patterned by photolithography and dry etching. Subsequently, plug-type W bottom-electrodes with thickness of 50 nm were fabricated by W-film deposition on the nanoholes and chemical mechanical planarization. In addition, 850 µL of a photoresist (AZ5214E) was spin-coated on the plug-type W patterned wafer at 5000 rpm for 30 s and soft baked at 120 °C for 1 min and 40 s to fabricate HfO_x-based ReRAM cells. Then, a photomask with 60×60 µm^2 patterns was aligned on the plug-type W-patterned wafer and exposed to UV light with a beam intensity of 20 mW cm^{-2} for 12 s. The exposed patterned photoresist was developed using a developer (AZ300MIF) for 70 s. The HfO_x switching layer with a thickness of ≈10 nm was deposited on the plug-type W bottom electrode patterned wafer, which had square-shaped photoresist patterns with dimensions of 60×60 µm^2 by sputtering the HfO_x target at RF with a power of 40 W under an Ar flow of 40 sccm. Subsequently, a top Pt electrode with a thickness of 50 nm was sputtered using a Pt target that was set at DC 30 W under an Ar flow of 30 sccm. Finally, the lift-off process was performed. Thus, the HfO_x-based ReRAM cells were completely fabricated with a vertical structure of a bottom W electrode with a diameter of 60 nm, HfO_x switching layer, and top Pt electrode. In addition, a similar photolithography process for 60×60 µm^2 photoresist patterns was conducted to fabricate CuO-based CBRAM cells. Then, the CuO resistive layer with a thickness of 10 nm was deposited on a plug-type W bottom electrode patterned wafer with square-shaped 60×60 µm^2 photoresist patterns by sputtering the CuO target at RF with a power of 90 W under an Ar flow of 40 sccm. Subsequently, a top Ag electrode with a thickness of 50 nm was thermally evaporated using Ag pellets at a pressure of 10^{-4} Pa, and a TiN top electrode with a thickness of 20 nm was sputtered using a TiN target at DC 40 W under an Ar flow of 30 sccm. Finally, N_2 annealing was performed 500 °C for 30 min after the lift-off process. Therefore, CuO-based CBRAM cells with a diameter of 60 nm were fabricated with a vertical structure of the bottom W electrode with a diameter of 60 nm, CuO resistive switching layer, top Pt, and TiN electrode. Finally, a similar photolithography process for 60×60 µm^2 photoresist patterns was performed to fabricate α-CO_x-based ReRAM cells. The α-CO_x switching layer with a thickness of 5 nm was deposited on a plug-type W bottom electrode patterned wafer for 60×60 µm^2 photoresist patterns by sputtering a graphite target at DC 250 W under an Ar flow of 10 sccm and various O_2 flows (i.e., 0 to 0.4, 0.8, 1.2, and 1.6 sccm) to adjust the partial pressure of oxygen corresponding to 0% to 3.8%, 7.4%, 10.7%, and 13.8%. Subsequently, a top Pt electrode with a thickness of 50 nm was sputtered using the Pt target at DC 30 W under an Ar flow of 30 sccm. Finally, a lift-off process was performed. The α-CO_x-based ReRAM cells were fabricated with a vertical structure of a bottom W electrode with a diameter of 60 nm, an α-CO_x resistive switching layer, and a top Pt electrode. Moreover, W bottom electrodes with a diameter of 60 nm were used for all three types of nonvolatile memories to compare the bi-stable resistance generation mechanism between binary metal oxide-based ReRAM cells, CBRAM cells, and α-CO_x-based ReRAM cells.

Fabrication of Micrometer Scale α-CO_x-Based ReRAM for Characterizing a Bi-Stable Resistance Generation Mechanism: A W film, which was the bottom electrode, with a thickness of 100 nm was sputtered on a SiO_2 film grown on a Si substrate using a W target at DC 40 W under an Ar flow of 30 sccm. Then, a similar photolithography process was conducted to produce square-shaped 60×60 µm^2 photoresist patterns. Then, the α-CO_x resistive switching layer with a thickness of 20 nm was deposited on the square-shaped 60×60 µm^2 photoresist patterns by sputtering a graphite target at DC 250 W under the Ar and O_2 flows of 10 and 1.2 sccm, respectively. Subsequently, the top Pt electrode with a thickness of 100 nm was sputtered using a Pt target at DC 30 W under an Ar flow of 30 sccm. After conducting the lift-off process, α-CO_x-based ReRAM cells with a memory cell area of 60×60 µm^2 were fabricated with a vertical structure of a W bottom electrode (≈100 nm), α-CO_x resistive switching layer (≈20 nm), and a Pt top electrode (≈100 nm). After a

© 2022 The Authors. Advanced Electronic Materials published by Wiley-VCH GmbH

pristine, reset after a set, and set after a reset, the depth profiles of the chemical composition of the α-CO_x-based ReRAM cells with a memory cell area of 60×60 µm^2 were analyzed using EELS, EDS, and XPS.

Material Characterization: The surface morphology of the plug-type W bottom electrode with a memory cell size diameter of ≈60 nm was investigated by atomic force microscopy (AFM, XE7). The crystallinity of the α-CO_x layer was observed using XRD (Rigaku SmartLab). The aberration-corrected STEM, EDS, and EELS (JEM-2100F) measurements were conducted with a beam energy of 200 keV. In addition, the EELS elemental mapping images of C-K and O-K edges were obtained at ≈0.66 nm pixel intervals. The XPS intensities of C—C sp^2, C—C sp^3, C=O, O—C=O, and O—(C=O)—O covalent bonds in the α-CO_x resistive layer were examined by XPS (K-Alpha+) using a monochromatic Al Kα X-ray source of 1486 eV. The GCIS was utilized for ion milling. The acceleration voltage of the GCIS (i.e., Ar_n^+ cluster) was 4 KeV and cluster size was 2000 (i.e., $n = 2000$) to minimize the chemical and structural damage to the α-CO_x resistive layer.

Electrical Measurements: The current–voltage (*I–V*) curves of the α-CO_x-based ReRAM cells were estimated using an Agilent B2902A semiconductor parameter analyzer. In addition, the reliability (i.e., write and erase endurance cycle) and switching speed measurements were performed using the Keithley 4200 A semiconductor parameter analyzer. The α-CO_x-based ReRAM cells were placed on a hot chuck where the temperature was regulated by a TAS 1000 temperature controller to measure the bi-stable resistance at a high operating temperature of 120–160 °C.

Supporting Information

Supporting Information is available from the Wiley Online Library or from the author.

Acknowledgements

This research was supported by the MOTIE (Ministry of Trade, Industry & Energy (10068055)) and KSRC (Korea Semiconductor Research Consortium) support program for the development of the future semiconductor device, BrainKorea21 Four.

Conflict of Interest

The authors declare no conflict of interest.

Data Availability Statement

The data that support the findings of this study are available from the corresponding author upon reasonable request.

Keywords

3D cross-point nonvolatile memories, bi-stable resistances, C—C sp^2 covalent bonds, C—C sp^3 covalent bonds, oxygenated amorphous carbon, resistive random-access memories

Received: October 7, 2021
Revised: December 18, 2021
Published online:

[1] R. F. Freitas, W. W. Wilcke, *IBM J. Res. Dev.* **2008**, *52*, 439.
[2] D. Waddington, M. Kunitomi, C. Dickey, S. Rao, A. Abboud, J. Tran, in *MEMSYS '19: Proc. Int. Symp. Memory Systems*, Association for Computing Machinery, New York **2019**, pp. 277–287, https://doi.org/10.1145/3357526.3357528.
[3] H.-Y. Cheng, F. Carta, W.-C. Chien, H.-L. Lung, M. J. BrightSky, *J. Phys. D: Appl. Phys.* **2019**, *52*, 473002.
[4] S. W. Fong, C. M. Neumann, H. S. P. Wong, *IEEE Trans. Electron Devices* **2017**, *64*, 4374.
[5] T. Kim, S. Lee, *IEEE Trans. Electron Devices* **2020**, *67*, 1394.
[6] L. Zhao, L. Jiang, Y. Zhang, N. Xiao, J. Yang, in *2017 18th Int. Symp. Quality Electronic Design*, IEEE, Piscataway, NJ **2017**, pp. 58–64, https://doi.org/10.1109/ISQED.2017.7918293.
[7] A. Kawahara, R. Azuma, Y. Ikeda, K. Kawai, Y. Katoh, Y. Hayakawa, K. Tsuji, S. Yoneda, A. Himeno, K. Shimakawa, T. Takagi, T. Mikawa, K. Aono, *IEEE J. Solid-State Circuits* **2013**, *48*, 178.
[8] M. Mao, P.-Y. Chen, S. Yu, C. Chakrabarti, *IEEE Trans. VLSI Syst.* **2017**, *25*, 1611.
[9] T. H. Lee, D. Y. Kang, T. G. Kim, *ACS Appl. Mater. Interfaces* **2018**, *10*, 33768.
[10] W. G. Kim, H. M. Lee, B. Y. Kim, K. H. Jung, T. G. Seong, S. Kim, H. C. Jung, H. J. Kim, J. H. Yoo, H. D. Lee, in *2014 Symp. VLSI Technology (VLSI-Technology): Digest of Technical Papers*, IEEE, Piscataway, NJ **2014**, pp. 1–2, https://doi.org/10.1109/VLSIT.2014.6894405.
[11] Y. Huai, H. Yang, X. Hao, Z. Wang, R. Malmhall, K. Sato, J. Zhang, D. H. Jung, X. Wang, P. Xu, in *IEEE Int. Memory Workshop (IMW)*, IEEE, Piscataway, NJ **2018**, pp. 1–4, https://doi.org/10.1109/IMW.2018.8388833.
[12] H. Yang, X. Hao, Z. Wang, R. Malmhall, H. Gan, K. Satoh, J. Zhang, D. H. Jung, X. Wang, Y. Zhou, in *IEEE Int. Electron Devices Meet*, IEEE, Piscataway, NJ **2017**, pp. 38.1.1–38.1.4, https://doi.org/10.1109/IEDM.2017.8268513.
[13] H. Aziza, M. Moreau, A. Pérez, A. Virazel, P. Girard, in *IEEE Int. New Circuits and Systems Conf. (NEWCAS)*, IEEE, Piscataway, NJ **2019**, pp. 1–4, https://doi.org/10.1109/NEWCAS44328.2019.8961278.
[14] J. Lin, J.-S. Yuan, in *IEEE Biomedical Circuits and Systems Conf. (BioCAS)*, IEEE, Piscataway, NJ **2017**, pp. 1–4, https://doi.org/10.1109/BIOCAS.2017.8325169.
[15] S. Lashkare, S. Chouhan, T. Chavan, A. Bhat, P. Kumbhare, U. Ganguly, *IEEE Electron Device Lett.* **2018**, *39*, 484.
[16] J. Lin, J.-S. Yuan, *Neurocomputing* **2020**, *375*, 102.
[17] K. Vishwakarma, R. Kishore, A. Datta, *ACS Appl. Electron. Mater.* **2020**, *2*, 3263.
[18] C. Bengel, F. Cuppers, M. Payvand, R. Dittmann, R. Waser, S. Hoffmann-Eifert, S. Menzel, *Front. Neurosci.* **2021**, *15*, 661856.
[19] Y. Shi, L. Nguyen, S. Oh, X. Liu, F. Koushan, J. R. Jameson, D. Kuzum, *Nat. Commun.* **2018**, *9*, 5312.
[20] S. Lim, M. Kwak, H. Hwang, *IEEE Trans. Electron Devices* **2018**, *65*, 3976.
[21] K. Wang, Q. Hu, B. Gao, Q. Lin, F.-W. Zhuge, D.-Y. Zhang, L. Wang, Y.-H. He, R. H. Scheicher, H. Tong, X.-S. Miao, *Mater. Horiz.* **2021**, *8*, 619.
[22] I. Sourikopoulos, S. Hedayat, C. Loyez, F. Danneville, V. Hoel, E. Mercier, A. Cappy, *Front. Neurosci.* **2017**, *11*, 123.
[23] X. Wu, V. Saxena, K. Zhu, S. Balagopal, *IEEE Trans. Circuits Syst. II: Express Briefs* **2015**, *62*, 1088.
[24] S. Dutta, V. Kumar, A. Shukla, N. R. Mohapatra, U. Ganguly, *Sci. Rep.* **2017**, *7*, 8257.
[25] R. C. Ivans, K. D. Cantley, J. L. Shumaker, in *IEEE 60th Int. Midwest Symp. Circuits and Systems (MWSCAS)*, IEEE, Piscataway, NJ **2017**, pp. 1125–1128, https://doi.org/10.1109/MWSCAS.2017.8053126.
[26] C. A. Santini, A. Sebastian, C. Marchiori, V. P. Jonnalagadda, L. Dellmann, W. W. Koelmans, M. D. Rossell, C. P. Rossel, E. Eleftheriou, *Nat. Commun.* **2015**, *6*, 8600.
[27] A. Rasool, R. Amiruddin, I. R. Mohamed, M. C. S. Kumar, *Superlattices Microstruct.* **2020**, *147*, 106682.

© 2022 The Authors. Advanced Electronic Materials published by Wiley-VCH GmbH

[28] T. Kim, H. Son, I. Kim, J. Kim, S. Lee, J. K. Park, J. Y. Kwak, J. Park, Y. Jeong, *Sci. Rep.* **2020**, *10*, 11247.
[29] J. H. Hur, *Sci. Rep.* **2020**, *10*, 5405.
[30] K. J. Heo, H. S. Kim, J. Y. Lee, S. J. Kim, *Sci. Rep.* **2020**, *10*, 9276.
[31] D. Lee, M. C. Chun, H. Ko, B. S. Kang, J. Kim, *Nanotechnology* **2020**, *31*, 245202.
[32] S. Maji, A. D. Paul, P. Das, S. Chatterjee, P. Chatterjee, V. R. Dhanak, A. K. Chakraborty, R. Mahapatra, *J. Mater. Sci.: Mater. Electron.* **2021**, *32*, 2936.
[33] J. H. Lee, J. H. Park, T. D. Dongale, T. G. Kim, *J. Alloys Compd.* **2020**, *821*, 153247.
[34] W.-M. Chung, Y.-F. Chang, Y.-L. Hsu, Y. C. D. Chen, C.-C. Lin, C.-H. Lin, J. Leu, *IEEE Trans. Device Mater. Reliab.* **2020**, *20*, 541.
[35] A. D. Paul, S. Biswas, P. Das, H. J. Edwards, V. R. Dhanak, R. Mahapatra, *IEEE Trans. Electron Devices* **2020**, *67*, 4222.
[36] S. Siegel, C. Baeumer, A. Gutsche, M. Witzleben, R. Waser, S. Menzel, R. Dittmann, *Adv. Electron. Mater.* **2020**, *7*, 2000815.
[37] R. V. Tominov, Z. E. Vakulov, V. I. Avilov, D. A. Khakhulin, A. A. Fedotov, E. G. Zamburg, V. A. Smirnov, O. A. Ageev, *Nanomaterials* **2020**, *10*, 1007.
[38] J. Lee, J. Kim, T. Kim, H. Sohn, *J. Mater. Sci.: Mater. Electron.* **2020**, *31*, 14384.
[39] A. Hazra, A. Tripathi, A. Jan, S. Kundu, P. K. R. Boppidi, *Nanotechnology* **2021**, *32*, 115201.
[40] K.-C. Kwon, M.-J. Song, K.-H. Kwon, H.-V. Jeoung, D.-W. Kim, G.-S. Lee, J.-P. Hong, J.-G. Park, *J. Mater. Chem. C* **2015**, *3*, 9540.
[41] K. Tsunoda, Y. Fukuzumi, J. R. Jameson, Z. Wang, P. B. Griffin, Y. Nishi, *Appl. Phys. Lett.* **2007**, *90*, 113501.
[42] M. Lanza, K. Zhang, M. Porti, M. Nafría, Z. Y. Shen, L. F. Liu, J. F. Kang, D. Gilmer, G. Bersuker, *Appl. Phys. Lett.* **2012**, *100*, 123508.
[43] S. Choi, S. H. Tan, Z. Li, Y. Kim, C. Choi, P. Y. Chen, H. Yeon, S. Yu, J. Kim, *Nat. Mater.* **2018**, *17*, 335.
[44] K.-H. Kwon, D.-W. Kim, H.-J. Kim, S.-M. Jin, D.-S. Woo, S.-H. Park, J.-G. Park, *J. Mater. Chem. C* **2020**, *8*, 8125.
[45] T. A. Bachmann, W. W. Koelmans, V. P. Jonnalagadda, M. L.e Gallo, C. A. Santini, A. Sebastian, E. Eleftheriou, M. F. Craciun, C. D. Wright, *Nanotechnology* **2018**, *29*, 035201.
[46] W. W. Koelmans, T. Bachmann, F. Zipoli, A. Ott, C. Dou, A. Ferrari, O. Cojocaru-Mirédin, S. Zhang, C. Scheu, M. Wuttig, V. K. Nagareddy, M. F. Cracium, A. M. Alexeev, C. D. Wright, V. P. Jonnalagadda, A. Curioni, A. Sebastian, E. Eleftheriou, in *2016 IEEE 8th International Memory Workshop (IMW)*, IEEE, Piscataway, NJ **2016**, pp. 1–4, https://doi.org/10.1109/IEDM.2008.4796740.
[47] S. D. Berger, D. R. McKenzie, P. J. Martin, *Philos. Mag. Lett.* **1988**, *57*, 285.
[48] F. Mangolini, J. B. McClimon, R. W. Carpick, *Anal. Chem.* **2016**, *88*, 2817.
[49] K. Haubner, J. Murawski, P. Olk, L. M. Eng, C. Ziegler, B. Adolphi, E. Jaehne, *ChemPhysChem* **2010**, *11*, 2131.
[50] N. Dwivedi, R. J. Yeo, N. Satyanarayana, S. Kundu, S. Tripathy, C. S. Bhatia, *Sci. Rep.* **2015**, *5*, 7772.
[51] J. Lin, S. Wang, H. Liu, *Electronics* **2021**, *10*, 731.
[52] W. Chen, R. Fang, M. B. Balaban, W. Yu, Y. Gonzalez-Velo, H. J. Barnaby, M. N. Kozicki, *Nanotechnology* **2016**, *27*, 255202.
[53] R. Xu, H. Jang, M. H. Lee, D. Amanov, Y. Cho, H. Kim, S. Park, H. J. Shin, D. Ham, *Nano Lett.* **2019**, *19*, 2411.
[54] K. Moon, S. Lim, J. Park, C. Sung, S. Oh, J. Woo, J. Lee, H. Hwang, *Faraday Discuss.* **2019**, *213*, 421.
[55] N. Xu, B. Gao, L. Liu, B. Sun, X. Liu, R. Han, J. Kang, B. Yu, in *2008 Symp. VLSI Technology*, IEEE, Piscataway, NJ **2008**, pp. 100–101, https://doi.org/10.1109/VLSIT.2008.4588578.
[56] X. Ding, Y. Feng, P. Huang, L. Liu, J. Kang, *Nanoscale Res. Lett.* **2019**, *14*, 157.
[57] X. Zhang, L. Xu, H. Zhang, J. Liu, D. Tan, L. Chen, Z. Ma, W. Li, *Nanoscale Res. Lett.* **2020**, *15*, 11.
[58] Y. Huang, Z. Shen, Y. Wu, X. Wang, S. Zhang, X. Shi, H. Zeng, *RSC Adv.* **2016**, *6*, 17867.
[59] H. Jiang, L. Han, P. Lin, Z. Wang, M. H. Jang, Q. Wu, M. Barnell, J. J. Yang, H. L. Xin, Q. Xia, *Sci. Rep.* **2016**, *6*, 28525.
[60] K. J. Gan, P. T. Liu, T. C. Chien, D. B. Ruan, S. M. Sze, *Sci. Rep.* **2019**, *9*, 14141.

© 2022 The Authors. Advanced Electronic Materials published by Wiley-VCH GmbH